NANO LETTERS

LETTER

pubs.acs.org/NanoLett

Graphene Magnetoresistance Device in van der Pauw Geometry

Jianming Lu, Haijing Zhang, Wu Shi, Zhe Wang, Yuan Zheng, Ting Zhang, Ning Wang, Zikang Tang,* and Ping Sheng*

Department of Physics and William Mong Institute of Nano Science and Technology, Hong Kong University of Science and Technology, Clear Water Bay, Kowloon, Hong Kong, China

Supporting Information

ABSTRACT: We have fabricated extraordinary magnetoresistance (EMR) device, comprising a monolayer graphene with an embedded metallic disk, that exhibits large room temperature magnetoresistance (MR) enhancement of up to 55 000% at 9 T. Finite element simulations yield predictions in excellent agreement with the experiment and show possibility for even better performance. Simplicity, ease of implementation and high sensitivity of this device imply great potential for practical applications.

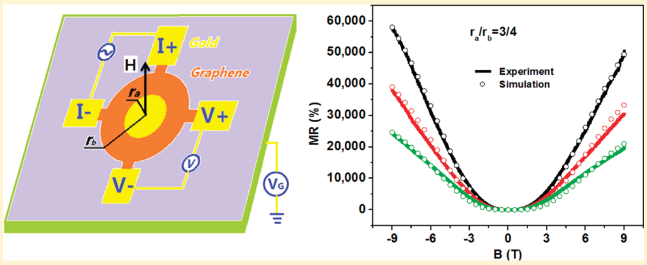

KEYWORDS: Graphene, extraordinary magnetoresistance, finite element simulations, magnetoresistance sensitivity

In contrast to the traditional giant magnetoresistance (GMR)[1] and colossal magnetoresistance (CMR)[2,3] devices in which the effects originate from material characteristics, extraordinary magnetoresistance (EMR) device[4−7] derives its effect from the geometric arrangement of nonmagnetic, high-mobility semiconductors with embedded metallic inhomogeneity. With high intrinsic mobility of up to 4 $m^2/(Vs)$,[8−10] graphene constitutes an ideal medium for EMR devices. It is therefore a natural extension to use graphene as the EMR medium. In this work, we show that the graphene EMR device can achieve geometric MR of up to 55 000% at 9 T with a potential for 500 000% in conjunction with a sensitivity that equals the best that has been reported so far.[11]

Weak localization for pure graphene[12−14] and strong localization for defective graphene,[15−19] both displaying negative MR, have been extensively studied at low temperatures. Negative MR has also been found in graphene nanoribbons up to room temperature.[20] Although intrinsic graphene has no MR at or far from the Dirac point, electron−hole puddles can give rise to a positive MR at room temperature, similar to the inhomogeneous semiconductors.[21] Recently, positive MR was also observed in thin graphite flakes.[22] In order to obtain high enough MR for potential applications, however, it is desirable to take advantage of graphene as a nonmagnetic high mobility semiconductor[23] for use in the EMR devices.

Figure 1a shows the schematic structure of our EMR device, and Figure 1b is a scanning electron microscope image of an actual device. The graphene film, mechanically exfoliated from natural graphite[8] and verified by Raman spectroscopy[24] to be monolayer, was first etched into the van der Pauw geometry by oxygen plasma. The electrodes and the concentric metal disk were formed by e-beam lithography with the metallic film, comprising 60 nm of Pd[25] or Ti/Au (3 nm/60 nm), formed by e-beam evaporation and subsequent lift-off. The radius of the metal disk is denoted as r_a and the outer radius of the graphene film is denoted by r_b. All electrical measurements were done in helium gas at 300 K in a Physical Property Measurement System with magnetic field up to 9 T. In order to remove the PMMA residues (leftover from the lift-off) and water adsorption, the device was heated up to 380 K for one hour before measurement.[26] The charge neutral point (CNP),[21] defined to be the gate voltage at which the resistance is maximum, was observed to be close to zero gate voltage after the heat treatment. The mobility of graphene, varying from 0.4 to 0.7 $m^2/(Vs)$,[8,10] was measured on the same graphene flake as those used in the EMR device.

In four-probe measurements, two adjacent electrodes (see Figure 1a for definition of "adjacent") were used for current injection and another two adjacent ones as voltage detectors. Since the geometry of our device is 4-fold symmetric, arbitrary adjacent pairs can be chosen with equal performance.[4] We define $R = (V_+ - V_-)/I$, and the magnetoresistance of the EMR device is defined as $MR = [R(B) - R(B=0)]/R(B=0)$.[11] Sensitivity of the EMR device is defined as the response of the output voltage (normalized by the injection current) to a unit magnetic field (in units of V/(AT) or Ω/T). The four-probe method has the advantage of eliminating contact resistance as well as the resistances from the arms that connect the electrodes to the graphene film.

The geometric nature of the MR effect in an EMR device is based on the observation that the MR is dependent on the ratio r_a/r_b, with both r_a/r_b = 0 (pure graphene) and r_a/r_b = 1 (conduction shorted by the metallic disk) being much smaller than those cases with intermediate values, as seen below. For reference, a sample with r_a/r_b = 1 has been fabricated to actually

Received: May 9, 2011
Revised: June 20, 2011
Published: June 22, 2011

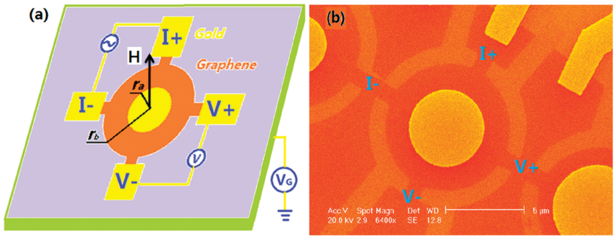

Figure 1. (a) Schematic illustration of the structure in our graphene EMR device. (b) A scanning electron microscope image (false color) of an actual EMR device. The two adjacent electrodes are for current injection ($I+$ and $I-$), whereas the other two are for voltage detection ($V+$ and $V-$). For two-terminal measurements, only $I+$ and $I-$ are used, both for current injection and for voltage detection.

verify that the resulting MR is similar to that of metal, that is, <5% at 9 T. We have also measured the MR of pure graphene flakes used in our experiments. They display MR varying from 300 to 500% under B = 9 T only near the CNP; otherwise no MR was observed. It follows that since these material MR values are orders of magnitude smaller than the EMR effect and that EMR depends on r_a/r_b as seen below, the EMR effect must be geometric in nature. This conclusion is further buttressed by simulation results showing the current path as a function of the magnetic field (see figures in the Supporting Information section), and the good agreement between theory and experiment, presented below.

In order to provide both theoretical understanding and support to the experimental results, numerical finite-element simulations were carried out by using the following equation derived from the force balance

$$\vec{j} \pm \mu \vec{j} \times \vec{B} = -\sigma \nabla \phi \qquad (1)$$

where ϕ is the electrical potential, $\vec{B}$ is the magnetic field normal to the planar device, σ is the conductivity, μ denotes mobility, and + in front of μ is for electrons and − for holes. It is understood that the material parameters σ and μ can take on different values σ_m, σ_g, μ_m, μ_g in the metallic and graphene regions, respectively. Details of the derivation, plus figures illustrating the EMR effect, are given in the Supporting Information section.

Figure 2 shows an EMR device with a diameter ratio r_a/r_b = 3/4. For this device we used Pd as the material of the central metallic disk. In the absence of an applied magnetic field, the resistance of the EMR device is 2.5 Ω, i.e., the contact resistance is minimal, since for a 60 nm Pd film in our geometry the resistance should be 1.75 Ω. At zero magnetic field, the resistance of our device displays almost no dependence on the gate voltage (inset to Figure 2a), since in the four probe geometry the central metallic disk provides a parallel channel of conduction with that through the graphene film. Through simulations whose results are shown in Figure 2b, it is found that a central metal disk resistance of 3 Ω yields best agreement with the experimental data. Since a small contact resistance is inevitable,[25,27] our experimental and theoretical values are considered to be in excellent agreement. Also, from simulations the conductivity at V_G = −8 V is 1.26 mS. Given that the mobility is 0.5 $m^2/(V\ s)$, the carrier density[28,29] is 1.6 × 10^{12} cm^{-2}. For V_G = −6 and −3 V, the simulated carrier density increases rapidly to 2.6 × 10^{12} and 4.5 × 10^{12} cm^{-2}, respectively.

To understand qualitatively the measured results, we consider two parts of the current path: one part that flows through the graphene and the other part which flows through the central metal disk. Relative ratio of these two parts of the total current determines the value of MR. In the absence of applied magnetic field, the current will flow mostly through the path of least resistance. As the metallic disk presents a region of high conductivity, current will tend to bypass the graphene region as much as possible. However, with increasing magnetic field, more and more current originally flowing through the metal disk will be deflected since the electric field (and hence the current) at the interface between the metallic disk and the graphene must be almost normal to the interface, owing to the large conductivity contrast between the two media, and the presence of the magnetic field gives rise to a Lorentz force that is perpendicular to the current (and hence the deflection). The part of the current flowing through the graphene film would thus increase at the expense of the other. This is shown graphically through the simulation results given in the Supporting Information section. As the conductivity of the graphene is much lower than that of the metallic disk, a geometric MR arises. Thus the conductance ratio σ_m/σ_g is a determining factor for the EMR devices.

In Figure 2b, the magnetoresistance below ±0.8 T is seen to be relatively small since the MR of the device is controlled by the metallic disk in this regime, and the metallic MR is small. Only

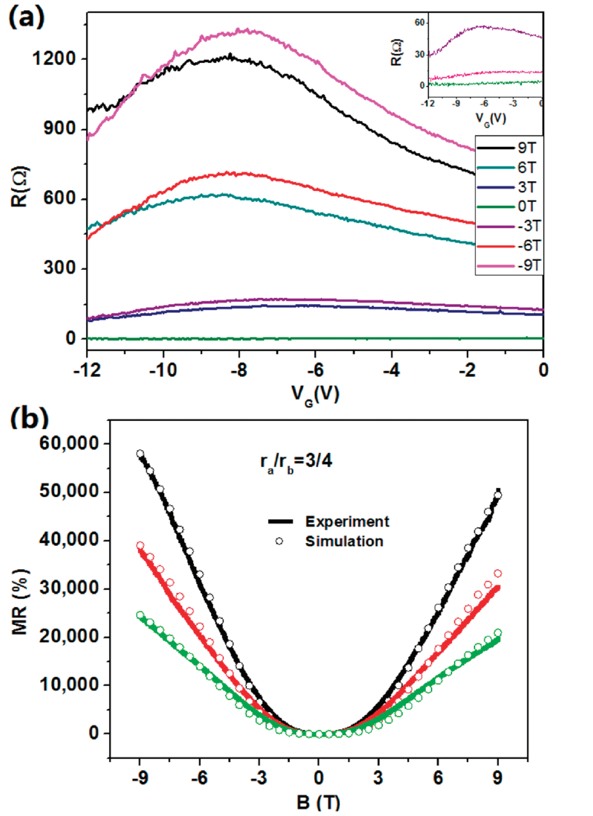

Figure 2. EMR device with a diameter ratio r_a/r_b = 3/4 and Pd as the metal for electrodes and the central metallic disk. (a) Resistance versus back gate under various magnetic fields. Inset: enlarged resistance at magnetic field 2, 1, 0 T (from top down). Gate voltage dependence is noted to almost disappears at zero magnetic field. (b) Magnetoresistance with different back gate voltages: V_G = −8, −6, −3 V (from the top down), solid curves are experimental data and empty circles denote the simulation results with the central disk misalignment error (determined via a SEM image of the actual device) taken into account.

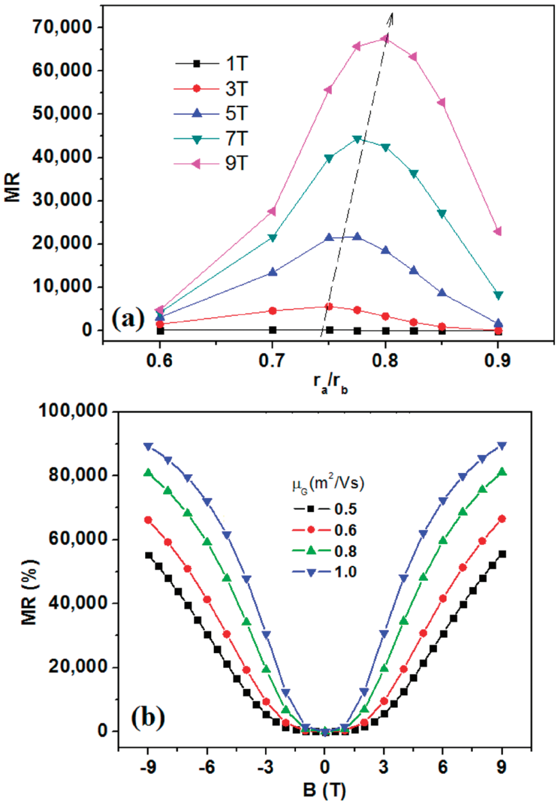

Figure 3. EMR performance simulations. (a) By varying the diameter ratio while keeping other parameters unchanged, we get MR with respect to diameter ratio under different magnetic field. Thus we can find optimized value of diameter ratio in different magnetic field (black dash arrow just for guidance of eyes). (b) Keep the diameter ratio unchanged and increase the graphene mobility up to 1.0 $m^2/(V\ s)$.

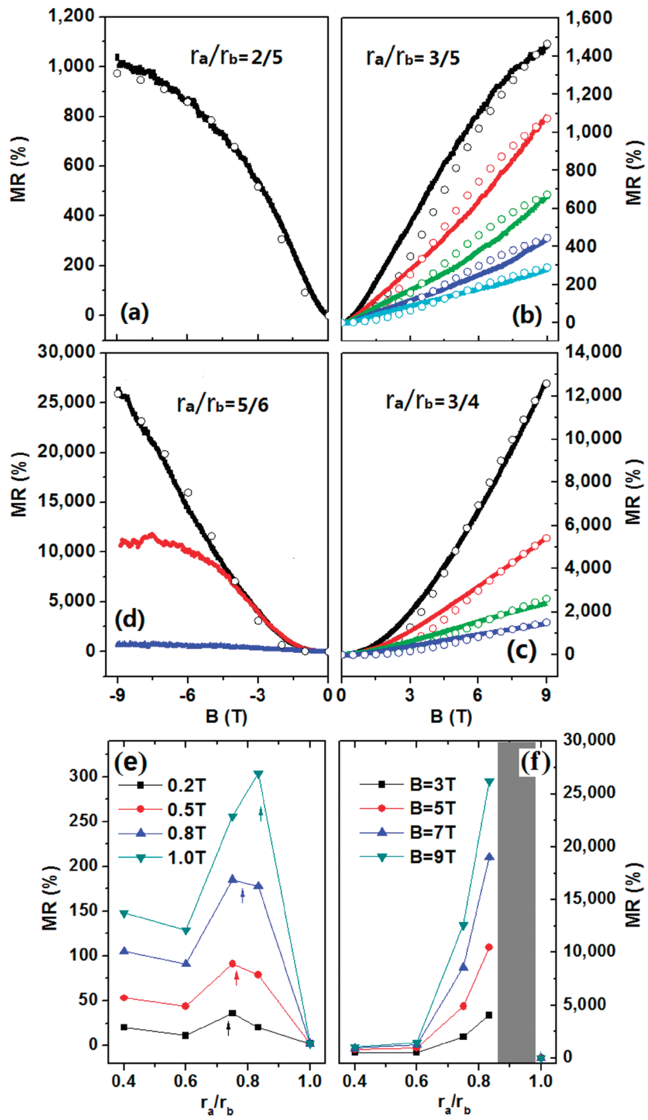

Figure 4. Magnetoresistance of four EMR devices with different diameter ratios r_a/r_b: (a) 2/5, measured at CNP only; (b) 3/5, measured at (from top down) $V_G = 0, -1, -2, -3$, and -4 V; (c) 3/4, measured at (from top down) $V_G = 0, -6, -12, -18$ V; and (d) 5/6, measured at (from top down) $V_G = 0, 2, 4$ V. Simulation results are indicated by open circles. The MR with respect to the diameter ratio under four different magnetic fields is summarized in (e,f). Colored arrows are the optimal values of the diameter ratios under the indicated magnetic fields. In (e), the optimal ratios for magnetic field up to 1 T are indicated by the arrows. For magnetic field larger than 1 T, shown in (f), optimized diameter ratios are clearly larger than 5/6 (in the gray region), since up to $r_a/r_b = 5/6$ the trend is still increasing, but at $r_a/r_b = 1$ the MR value is close to the horizontal axis.

when the magnetic field is sufficiently large to deflect the current from the central metallic disk will the resistance of the EMR device rise rapidly. As the back gate voltage (V_G) deviates from the CNP (denoted as V_D), the carrier density (and hence the conductivity) of graphene increases. Given that the conductance of metal disk is unchanged, the conductance ratio σ_m/σ_g is thereby lowered for the red ($V_G - V_D = 2$ V) and green ($V_G - V_D = 5$ V) curves, and so do their MR values. This agrees well with our analysis. This gate-tunable capability thus allows us to obtain the maximum MR for a specific EMR device.

The reason of the slight asymmetry in the observed MR (with respect to the up−down direction of the applied magnetic field) shown in Figure 2b is the alignment error of the central metal disk, owing to imperfection in e-beam lithography and the undercut during etching by O_2 plasma.. This is verified by our simulations (for details see the Supporting Information section) in which the input alignment error was determined via a SEM image of the actual device. The size of the off-center error has been measured to be on the order of tens of nanometers. With the experimental alignment error taken into account, excellent theory−experiment agreement is obtained.

We use simulations to first explore the dependence of the EMR effect on the r_a/r_b ratio and the grapheme mobility to be followed by experimental results. In Figure 3a, we show that the optimal r_a/r_b ratio varies as a function of the applied magnetic field with higher ratio preferred under high magnetic field.[4] Here the simulations were carried out by varying the diameter ratio while keeping constant other parameter values such as the graphene mobility ($\mu_g = 0.5\ m^2/(Vs)$) and the conductance of the central metal disk ($\sigma_m = 0.33$ S). In Figure 3b, we show that by keeping the diameter ratio at 3/4, much higher MR is obtained if the graphene mobility is increased from 0.5 $m^2/(Vs)$ to a potential value of 1.0 $m^2/(Vs)$.[9,30] It is noted that the effect of increasing the mobility is much more significant under a low magnetic field than that under a high magnetic field. This is due to the fact that in eq 1, mobility always appears in the product form with the magnetic field, and that the MR effect saturates at large magnetic field.

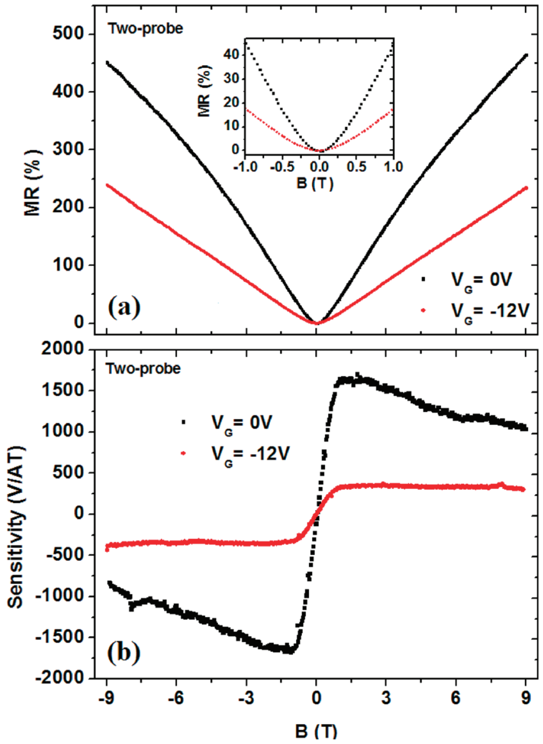

Figure 5. Two-terminal measurements of an EMR device with r_a/r_b = 3/4 at two gate voltages V_G = 0 and V_G = −12 V, plotted as a function of applied magnetic field. MR is shown in (a), where the inset shows the small field region behavior, and sensitivity is shown in (b).

Figure 4a−d shows the magnetoresistance of four EMR devices with four different filling ratios r_a/r_b = 2/5 (a), 3/5 (b), 3/4 (c), and 5/6 (d). These samples were fabricated by using Au as the metal for the central disk with a thin Ti adhesion layer. From Figure 4, the performance of the EMR devices is clearly seen to be related to r_a/r_b. For devices with relatively small r_a/r_b, for example, those shown in Figure 4a,b, MR saturates at a relatively low field. While for devices whose MR are shown in Figure 4c,d, the MR saturation is not observed at V_G = 0 even at 9 T. For V_G = 0, we can see that under 9 T of magnetic field the MR increases from 1000% to 26 000% when r_a/r_b varies from 2/5 to 5/6.

With the four available samples, the magnetic field dependence of the optimal r_a/r_b ratio can already be tested against theory prediction, albeit only at low magnetic fields. This is shown in Figure 4e. Here the arrows show the optimal diameter ratio. Good theory-experiment agreement is seen when compared with the predictions shown in Figure 3a.

To avoid obscuring the details under a small magnetic field, the MR shown in Figure 4e is only up to 1 T. The MR curves with respect to r_a/r_b under B > 1 T are presented in Figure 4f in which the optimal values are expected to be in the gray region, since up to the ratio of r_a/r_b = 5/6 the MR values are still increasing but at r_a/r_b = 1 we know the value to be close to the horizontal axis.

Simulations were carried out for the four samples (with embedded Au disks) with various r_a/r_b ratios shown in Figure 4 (results shown by open circles). While reasonable fittings were obtained, the required metal conductance values used in the fittings, ranging from 15 to 60 mS, are noted to be much lower than the 2.71 S for the conductance of a 60 nm Au film. In view of the good agreement between theory and experimental conductance values obtained for the Pd-disk sample (Figure 2), this discrepancy is attributed to the large contact resistance between the Ti/Au disk and the graphene that is in series with the resistance of the disk. The contact resistance deduced from comparisons between our data and the fitting values, on the order of $1-2 \times 10^{-6}\ \Omega\cdot\mathrm{cm}^2$, are consistent with those reported in ref 27, ranging from 10^{-7} to $10^{-4}\ \Omega\cdot\mathrm{cm}^2$. A more detailed comparison of the MR results with and without the contact resistance is given in the Supporting Information, part 5.

Devices shown in Figures 2b and Figure 4c are noted to have similar graphene mobility (μ_g = 0.5 m^2/(Vs)) and diameter ratio (3/4), but they nevertheless behave very differently. This is precisely because σ_m (including the contact resistance) plays an important role in the EMR performance. Besides the metallic disk conductance, the graphene mobility can also play an important role (as the metallic mobility μ_m is always much lower, only μ_g has a significant effect on the MR). For the two samples shown in Figures 4c,d, the diameter ratios (0.75 in panel c and 0.83 in panel d) are both fairly close to the optimal value of 0.8 at 9 T (see Figure 3a). But at 9 T the MR value in Figure 4d is about 25 000%, almost double that of Figure 4c. From our simulation fittings to the data, this difference is attributed to the higher mobility μ_g = 1.0 m^2/(Vs) for the sample in Figure 4d, which is higher than that for the sample in Figure 4c, with a fitted mobility value of μ_g = 0.5 m^2/(Vs). Both values are noted to be within the observed range for graphene (although the 1.0 m^2/(Vs) value is slightly higher than those we measured in our samples).

Our graphene EMR devices display the tunability of carrier density[23] via the gate voltage. This is clearly shown in Figure 4b−d, as noted previously. This tunability can compensate to some extent the sample differences that arise from the fabrication process.

For consideration of easy fabrication, fewer electrodes are generally preferred.[4,11,23] We have tested the performance of the same EMR device shown in Figure 4c by using only I+ and I− electrodes as indicated in Figure 1a. Because there are arms connecting the graphene ring and metal electrodes, the resulting MR performance is reduced because here the graphene arms are considered in series with the EMR device. For the two-probe device, the MR and its sensitivity as functions of the magnetic field are shown in Figures 5a,b, respectively. It is seen that while the MR is much lower than that of the four-probe device, the sensitivity is much higher, owing to the contribution of the resistance from the graphene arms. Our two-terminal EMR device's sensitivity is above 1000 V/(AT), comparable to the best values that have been reported.[11,23] We thus conclude that with optimization of device geometry and enhancement of graphene quality and metallic conductivity, the graphene EMR device can offer great potential for practical applications.

■ ASSOCIATED CONTENT

Supporting Information. Additonal information and figures. This material is available free of charge via the Internet at http://pubs.acs.org.

■ AUTHOR INFORMATION

Corresponding Author
*E-mail: (Z.T.) phzktang@ust.hk; (P.S.) sheng@ust.hk.

■ ACKNOWLEDGMENT

H.J.Z. wishes to thank Z. L. Xu and J. Mei for the help provided in COMSOL simulations. This work is supported by

Research Grant Council of Hong Kong Grants HKUST9/CRF/08 and HKUST 603108. Technical support of the electron-beam lithography facility at MCPF (Project No. SEG_HKUST08) is hereby acknowledged.

■ REFERENCES

(1) Egelhoff, W. F.; Ha, T.; Misra, R. D. K.; Kadmon, Y.; Nir, J.; Powell, C. J.; Stiles, M. D.; McMichael, R. D. *J. Appl. Phys.* **1995**, *78*, 273.

(2) Rao, C. N. R.; Raveau, B. *Colossal Magnetoresistance,Charge Ordering and Related Properties of Manganese Oxides*; World Scientific: Singapore, 1998.

(3) Jin, S.; McCormack, M.; Tiefel, T. H. *J. Appl. Phys.* **1994**, *76*, 6929.

(4) Solin, S. A.; Thio, T.; Hines, D. R.; Heremans, J. J. *Science* **2000**, *289*, 1530.

(5) Moussa, J.; Ram-Mohan, L. R.; Sullivan, J.; Zhou, T.; Hines, D. R.; Solin, S. A. *Phys. Rev. B* **2001**, *64*, 184410.

(6) Solin, S. A.; Hines, D. R.; Rowe, A. C. H.; Tsai, J. S.; Pashkin, Y. A.; Chung, S. J.; Goel, N.; Santos, M. B. *Appl. Phys. Lett.* **2002**, *80*, 4012.

(7) Solin, S. A.; Hines, D. R.; Rowe, A. C. H.; Tsai, J. S.; Pashkin, Y. A. *J. Vac. Sci. Technol., B* **2003**, *21*, 3002.

(8) Geim, A. K.; Novoselov, K. S. *Nat. Mater.* **2007**, *6*, 183.

(9) Dean, C. R.; Young, A. F.; Meric, I.; Lee, C.; Wang, L.; Sorgenfrei, S.; Watanabe, K.; Taniguchi, T.; Kim, P.; Shepard, K. L.; Hone, J. *Nat. Nanotechnol.* **2010**, *5*, 722.

(10) Chen, J. H.; Jang, C.; Xiao, S.; Ishigami, M.; Fuhrer, M. S. *Nat. Nanotechnol.* **2008**, *3*, 206.

(11) Boero, G.; Demierre, M.; Besse, P. A.; Popovic, R. S. *Sens. Actuators, A* **2003**, *106*, 314.

(12) Tikhonenko, F. V.; Horsell, D. W.; Gorbachev, R. V.; Savchenko, A. K. *Phys. Rev. Lett.* **2008**, *100*, 056802.

(13) Gorbachev, R. V.; Tikhonenko, F. V.; Mayorov, A. S.; Horsell, D. W.; Savchenko, A. K. *Phys. Rev. Lett.* **2007**, *98*, 176805.

(14) Morozov, S. V.; Novoselov, K. S.; Katsnelson, M. I.; Schedin, F.; Ponomarenko, L. A.; Jiang, D.; Geim, A. K. *Phys. Rev. Lett.* **2006**, *97*, 016801.

(15) Elias, D. C.; Nair, R. R.; Mohiuddin, T. M. G.; Morozov, S. V.; Blake, P.; Halsall, M. P.; Ferrari, A. C.; Boukhvalov, D. W.; Katsnelson, M. I.; Geim, A. K.; Novoselov, K. S. *Science* **2009**, *323*, 610.

(16) Gómez-Navarro, C.; Weitz, R. T.; Bittner, A. M.; Scolari, M.; Mews, A.; Burghard, M.; Kern, K. *Nano Lett.* **2007**, *7*, 3499.

(17) Bostwick, A.; McChesney, J. L.; Emtsev, K. V.; Seyller, T.; Horn, K.; Kevan, S. D.; Rotenberg, E. *Phys. Rev. Lett.* **2009**, *103*, 056404.

(18) Kaiser, A. B.; Gómez-Navarro, C.; Sundaram, R. S.; Burghard, M.; Kern, K. *Nano Lett.* **2009**, *9*, 1787.

(19) Moser, J.; Tao, H.; Roche, S.; Alzina, F.; Sotomayor Torres, C. M.; Bachtold, A. *Phys. Rev. B* **2010**, *81*, 205445.

(20) Bai, J.; Cheng, R.; Xiu, F.; Liao, L.; Wang, M.; Shailos, A.; Wang, K. L.; Huang, Y.; Duan, X. *Nat. Nanotechnol.* **2010**, *5*, 655.

(21) Guttal, V.; Stroud, D. *Phys. Rev. B* **2005**, *71*, 201304(R).

(22) Vansweevelt, R.; Mortet, V.; D'Haen, J.; Ruttens, B.; Van Haesendonck, C.; Partoens, B.; Peeters, F. M.; Wagner, P. *Phys. Status Solidi A* **2011**, *208*, 1252.

(23) Pisana, S.; Braganca, P. M.; Marinero, E. E.; Gurney, B. A. *Nano Lett.* **2010**, *10*, 341.

(24) Ferrari, A. C.; Meyer, J. C.; Scardaci, V.; Casiraghi, C.; Lazzeri, M.; Mauri, F.; Piscanec, S.; Jiang, D.; Novoselov, K. S.; Roth, S.; Geim, A. K. *Phys. Rev. Lett.* **2006**, *97*, 187401.

(25) Xia, F.; Perebeinos, V.; Lin, Y.-m.; Wu, Y.; Avouris, P. *Nat. Nanotechnol.* **2011**, *6*, 179.

(26) Stolyarova, E.; Rim, K. T.; Ryu, S.; Maultzsch, J.; Kim, P.; Brus, L. E.; Heinz, T. F.; Hybertsen, M. S.; Flynn, G. W. *Proc. Natl. Acad. Sci. U. S.A.* **2007**, *104*, 9209.

(27) Robinson, J. A.; LaBella, M.; Zhu, M.; Hollander, M.; Kasarda, R.; Hughes, Z.; Trumbull, K.; Cavalero, R.; Snyder, D. *Appl. Phys. Lett.* **2011**, *98*, 053103.

(28) Martin, J.; Akerman, N.; Ulbricht, G.; Lohmann, T.; Smet, J. H.; von Klitzing, K.; Yacoby, A. *Nat. Phys.* **2008**, *4*, 144.

(29) Bolotin, K. I.; Sikes, K. J.; Hone, J.; Stormer, H. L.; Kim, P. *Phys. Rev. Lett.* **2008**, *101*, 096802.

(30) Lafkioti, M.; Krauss, B.; Lohmann, T.; Zschieschang, U.; Klauk, H.; Klitzing, K. v.; Smet, J. H. *Nano Lett.* **2010**, *10*, 1149.

Supporting Information

1. Finite Element Analysis using COMSOL Multiphysics

The governing equations are the magnetostatic condition

$$\nabla \cdot \vec{j} = 0, \tag{1}$$

where $\vec{j}$ is the current density, and the force balance condition

for holes:

$$\vec{j} - \mu \vec{j} \times \vec{B} = -\sigma \nabla \phi \ , \tag{2-a}$$

for electrons:

$$\vec{j} + \mu \vec{j} \times \vec{B} = -\sigma \nabla \phi \ , \tag{2-b}$$

where ϕ is the electrical potential, $\vec{B}$ is the magnetic field normal to the planar device, σ is the conductivity, and μ denotes mobility. It is understood that the material parameters σ and μ can take on different values σ_m, σ_g; μ_m, μ_g in the metallic and graphene regions, respectively.

Equation (2-a) and (2-b) can be shown to result from the balance of the dissipative force and the Lorentz force given by (in SI units),

$$m\vec{v} / \tau = q\vec{E} + q\vec{v} \times \vec{B}, \tag{3}$$

where *m* denotes the electron mass, τ the mean collision time, $\vec{v}$ the drift velocity, $q \cong 1.6\times10^{-19} C$ for holes and $q \cong -1.6\times10^{-19} C$ for electrons. For holes, the equivalence of Eqs. (2-a) and (3) is achieved by identifying $\sigma = nq^2\tau / m$, $\mu = q\tau / m$, $\vec{E} = -\nabla\phi$, and $\vec{j} = nq\vec{v}$. Here *n* denotes the charge carrier density. For electrons, the equivalence of Eqs. (2-b) and (3) is achieved by identifying $\sigma = nq^2\tau / m$, $\mu = -q\tau / m$, $\vec{E} = -\nabla\phi$, and $\vec{j} = nq\vec{v}$.

The boundary condition is given by $j_n = 0$, except at the two current leads where the injection current is specified.

In Fig. S1, we use the simulation to illustrate the working principle of an EMR device.

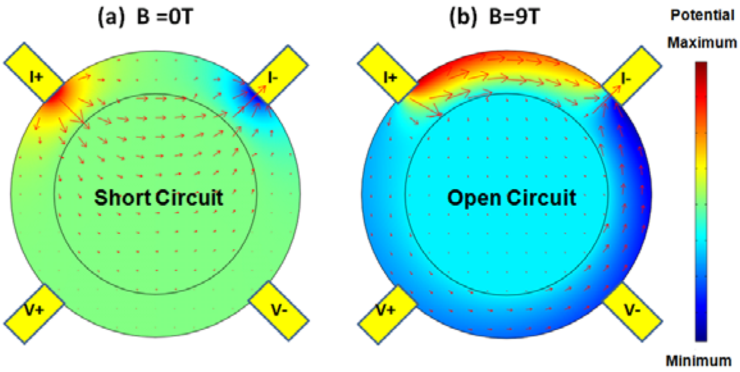

FIG. S1 Current/potential distribution of a composite with van der Pauw geometry comprising a metallic disk embedded in a monolayer of graphene. In (a) and (b), the red arrows represent the current direction and the color inside the disks represents the potential.

2. Asymmetry of the magnetoresistance with respect to the magnetic field direction

In Fig. S2(a), we show a SEM image of the EMR device whose performance is given in Fig. 2. The two red circles denote the positions of the circular graphene flake and the central Pd disk. It is clear that they are not perfectly concentric, and the Pd disk is off-center somewhat. In Figs. S2(b) and S2(c) we show the two cases in which (b) uses the actual position data as shown in S2(a) and (c) assumes perfect concentric positioning. The difference is clearly seen, and (b) gives a much better fitting to the data.

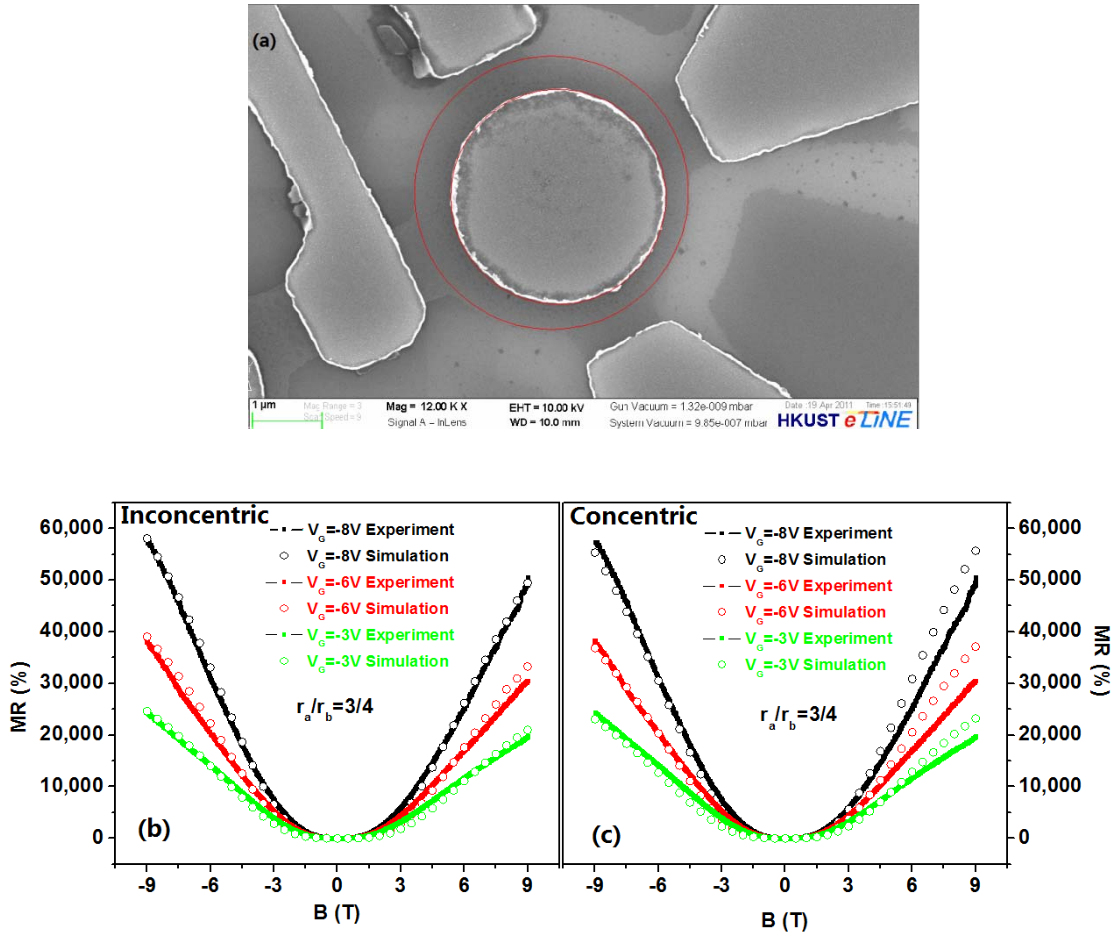

FIG. S2 (a) SEM picture of an actual EMR device used for Fig. 2. Two red circles indicate central metal disk and the underlying graphene film respectively. It is clear that the two circles are not concentric. (b) Using model exactly the same with SEM picture, we simulate the EMR performance, which is in agreement with experimental results. (c) We assume the two circles perfectly concentric in the simulation model and use the same simulation parameters. Agreement with the measured data becomes poorer. This comparison helps us to understand the reason for the asymmetry seen in the magnetoresistance data with respect to the magnetic field direction.

3. Quadratic behavior of the MR under low magnetic field

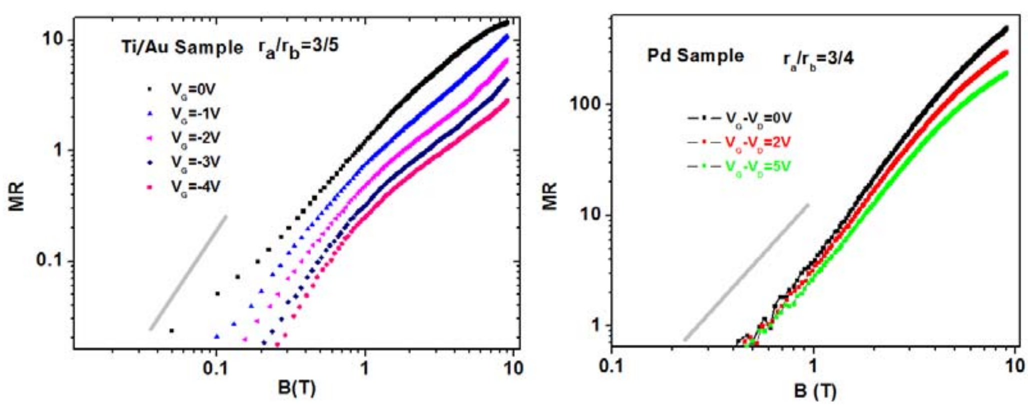

FIG. S3 (a) A log-log plot of Fig. 4(b) for one of the EMR samples with the Ti/Au metallic disk. (b) A log-log plot of Fig. 2(b) the the EMR sample with the Pd metallic disk. Grey lines in (a) and (b) have a slope of 2 for visual guidance.

4. Magnetoresistance away from the charge neutrality point

At the charge neutral point (V_G=V_D), resistance gets its maximal value in a certain magnetic field. When V_G >V_D (electron) or V_G <V_D (hole), resistance decreases.

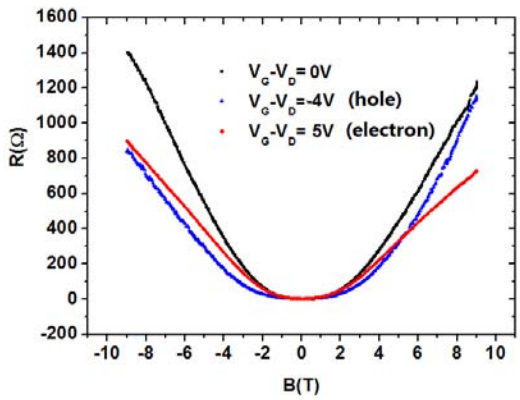

FIG. S4 Resistance of the device whose MR performance is shown in Fig. 2, plotted versus the magnetic field. Different curves represent varying amount of deviations from the CNP.

5. Contact resistance between the Ti/Au film and graphene

The Ti/Au film can detach easily from grapheme, but it adheres well to SiO_2. We have improved the contact by etching a hole (with a diameter smaller than that of the metal disk) at the center of the graphene disk so that the SiO_2 contacts directly the Ti/Au film. Thus the contact area of metal disk and graphene, e.g., in the case of r_a/r_b=3/4 shown in Fig. 4(c), is about 4.8 μm^2. Reference [27] has given the contact resistivity for graphene and Ti/Au film to range from 10^{-7} to 10^{-4} Ω cm^2. If we choose an in-between value of 10^{-6} Ω cm^2, then the contact resistance for our samples can be estimated to be (10^{-6} Ω cm^2)/(4.8 μm^2) = 20.8 Ω . This value, when combined with the resistance of a 60 nm thick Au disk, leads to a conductance of 47.2 mS, which is consistent with our fitting values, which range from 15-60 mS.

Alternatively, we can derive the contact resistivity in our samples to be in the range of 1-2$\times 10^{-6}$ Ω cm^2. These values are consistent with those given in Ref. [27].

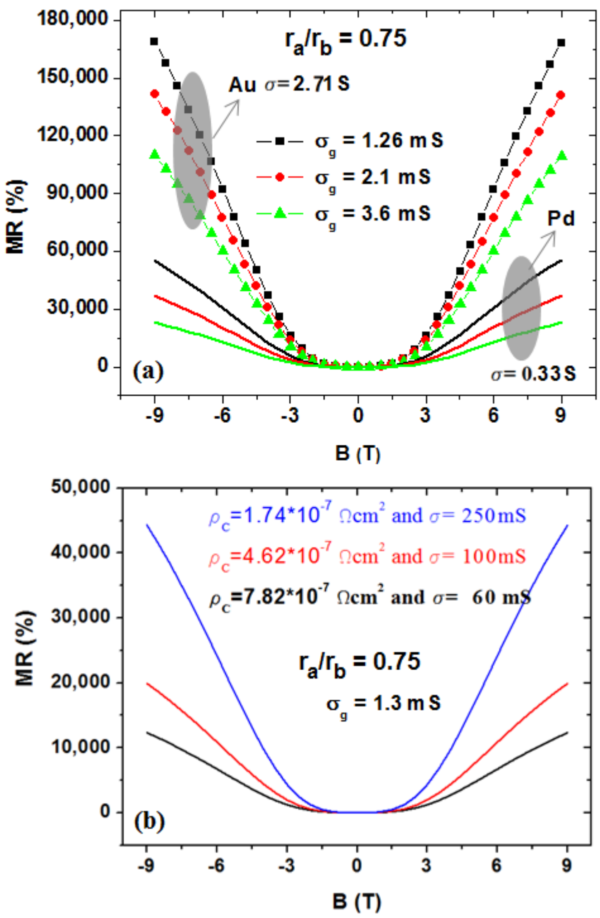

FIG. S5 (a) Comparison of simulated EMR device performances without the contact resistance, in combination with three different graphene conductances (indicated by the three different colors of the curves), and the actual device (with parameters the same as those for the device with the Pd metallic disk shown in Fig. 2). In (b), the graphene conductance is set at 1.3 mS, but the metal disk conductance and the corresponding contact resisitivity are varied. The black curve is noted to be the best fit to the data shown in Fig. 4(c).

If we can reduce the contact resistivity between Ti/Au and graphene from 10^{-6} Ω cm^2 to 10^{-7} Ω cm^2, the lowest reported value, then the metal disk conductance would be 0.41 S. This can lead to an EMR device performance shown in Fig. 2, where the effective conductance is about 0.33 S (for the Pd disk). Only if the contact resistance is zero, which is an idealized case, can we get $\sigma_m = 2.71$ S. Comparison between this idealized case and the device using the Pd disk ($\sigma_m = 0.33$ S) are shown in Fig. S5(a). In Fig. S5(b), simulated MR performance under three different combinations of the metal disk conductivity (shown as the value of σ used in the COMSL simulation) and contact resistance (ρ_c) are shown. The black curve, with parameter values of σ=60 mS and a corresponding contact resistivity of 7.8*10^{-7} Ω cm^2, corresponds to the best fit to the data shown in Fig. 4(c).